HHS Public Access

Author manuscript

Nat Photonics. Author manuscript; available in PMC 2016 September 16.

Published in final edited form as:

Nat Photonics. 2014 September ; 8(9): 723–730. doi:10.1038/nphoton.2014.166.

Through-skull fluorescence imaging of the brain in a new near-infrared window

Guosong Hong[1,5], **Shuo Diao**[1,5], **Junlei Chang**[2,5], **Alexander L. Antaris**[1], **Changxin Chen**[1], **Bo Zhang**[1], **Su Zhao**[1], **Dmitriy N. Atochin**[3], **Paul L. Huang**[3], **Katrin I. Andreasson**[4], **Calvin J. Kuo**[2], and **Hongjie Dai**[1]

[1]Department of Chemistry, Stanford University, Stanford, California 94305, USA.

[2]Division of Hematology, School of Medicine, Stanford University, Stanford, California 94305, USA.

[3]Cardiovascular Research Center and Cardiology Division, Massachusetts General Hospital, Harvard Medical School, Charlestown, Massachusetts 02129, USA.

[4]Department of Neurology and Neurological Sciences, Stanford University Medical Center, Stanford, California 94305, USA.

Abstract

To date, brain imaging has largely relied on X-ray computed tomography and magnetic resonance angiography with limited spatial resolution and long scanning times. Fluorescence-based brain imaging in the visible and traditional near-infrared regions (400–900 nm) is an alternative but currently requires craniotomy, cranial windows and skull thinning techniques, and the penetration depth is limited to 1–2 mm due to light scattering. Here, we report through-scalp and through-skull fluorescence imaging of mouse cerebral vasculature without craniotomy utilizing the intrinsic photoluminescence of single-walled carbon nanotubes in the 1.3–1.4 micrometre near-infrared window. Reduced photon scattering in this spectral region allows fluorescence imaging reaching a depth of >2 mm in mouse brain with sub-10 micrometre resolution. An imaging rate of ~5.3 frames/s allows for dynamic recording of blood perfusion in the cerebral vessels with sufficient temporal resolution, providing real-time assessment of blood flow anomaly in a mouse middle cerebral artery occlusion stroke model.

Introduction

The essential functions of the brain dictate that any significant cerebral dysfunction or disease, such as the cerebrovascular disease, could lead to severe morbidity or mortality.[1]

Correspondence and requests for materials should be addressed to H.D. (hdai@stanford.edu) or C.J.K. (cjkuo@stanford.edu).

[5]These authors contribute equally to this work.

Author contributions

H.D., C.J.K., G.H., S.D., and J.C. conceived and designed the experiments. G.H., S.D., J.C., A.L.A., C.C., B.Z., S.Z. and D.N.A. performed the experiments. G.H., S.D., J.C., A.L.A., C.C., B.Z., S.Z., D.N.A., P.L.H., K.I.A., C.J.K. and H.D. analyzed the data and wrote the manuscript. All authors discussed the results and commented on the manuscript.

Brain imaging has relied on X-ray computed tomography (CT) and magnetic resonance angiography (MRA) to reach sufficient penetration depth,[2–4] but these modalities are limited in spatial resolution (~ sub-millimeter) and long scanning times (~ minutes),[5–7] impairing the resolution of small vessels and dynamic blood flow in the brain. On the other hand, fluorescence-based optical imaging of the brain in the visible and traditional near-infrared regions (400–900 nm) has relied on craniotomy, cranial windows and skull thinning techniques[8–11] and the penetration depth for *in vivo* brain imaging has been limited to a depth of 1–2 mm[8,12–14] by light scattering.[15,16]

Recently, we and others have shown that biological imaging with carbon nanotube and quantum dot fluorescent agents in the long near-infrared region (1.0–1.7 μm, named NIR-II region) can benefit from reduced tissue scattering and autofluorescence, reaching deeper penetration depths *in vivo* than traditional NIR (NIR-I, 750–900 nm) imaging techniques.[17–29] Photon scattering scales as $\lambda^{-\alpha}$, where α = 1.2 to 4 for biological tissues. The reduced scattering in the NIR-II region has allowed *in vivo* fluorescence imaging of blood vessels in the hindlimb of mice with ~30 μm lateral resolution at > 1 mm depth.[22] Here, we report the first non-invasive brain imaging in a narrow 1.3–1.4 μm region (named as the NIR-IIa region), allowing penetration through intact scalp and skull and resolving cerebral vasculatures with a previously unattainable spatial resolution of sub-10 μm at a depth of >2 mm underneath the surface of the scalp skin in an epifluorescence imaging mode. The 1.3–1.4 μm NIR-IIa window is rationally chosen for *in vivo* imaging so as to minimize scattering by rejecting shorter wavelength photons than 1.3 μm while avoiding increase light absorption by water vibrational overtone modes above ~1.4 μm. Further, dynamic NIR-IIa cerebrovascular imaging with high temporal resolution (< 200 ms/frame) was used to reveal drastically reduced blood flow due to arterial occlusion in an acute stroke model on mice.

Results

Phantom Imaging in NIR-I, NIR-II and NIR-IIa Regions

We first used a highly scattering medium (Intralipid ®, 1 wt% aqueous solution) as a mimic to biological tissue[20] and studied the penetration depths of fluorescence imaging in the NIR-I (<900 nm), NIR-II (1.0–1.7 μm) and NIR-IIa (1.3–1.4 μm) regions. High pressure CO conversion (HiPCO) single-walled carbon nanotube[30] (SWNT)-IRDye800 conjugates excited by an 808-nm laser were used as emitters fluorescing in a wide 800 – 1700 nm span (for side-by-side comparing imaging with IRDye800 that emits in the 800–900 nm NIR-I window, and with SWNT that emits in the 1000–1700 nm NIR-II window),[31,32] using optical filters to select detection and imaging wavelength ranges (Fig. 1a). When a capillary tube filled with the SWNT-IRDye800 solution was immersed in an Intralipid solution at 1 mm depth, sharp images were obtained in all three spectral windows (Fig. 1b, top). However, when the sample immersion depth increased to 1 cm in Intralipid, scattering of photons became obvious in the entire NIR-II (1.0–1.7 μm) region and was more severe in the NIR-I (< 900 nm) region, causing the image of the capillary tube to be smeared and invisible (Fig. 1b, bottom). In contrast, an image taken in the 1.3–1.4 μm NIR-IIa region resolved sharp edges of the capillary tube even at 1 cm immersion depth in Intralipid (Fig. 1b bottom

right image), suggesting reduced scattering. The observed wavelength dependence of phantom imaging (Fig. 1b & S1) could be rationalized by considering the measured scattering coefficient vs. wavelength for 1% Intralipid (red curve, Fig. 1c, in agreement with previously reported reduced scattering coefficient of $\mu_s^{'}=1.6\lambda^{-2.4}$, blue curve. In this case, and those to follow, $\mu_s^{'}$ is the scattering coefficient in mm^{-1} and λ is the wavelength in μm, with the prefactor in appropriate unit to make units consistent on both sides of the equation).[33] The curves exhibited photon scattering scaling inversely proportional with wavelength. Rejecting shorter wavelength photons below 1.3 μm led to drastically improved imaging by avoiding feature smearing and background signals caused by scattering of short-wavelength photons. The increased absorption in the >1.4-μm region (peak shown in Fig. 1c) was due to light excitation of the first overtone vibration of water molecules in the Intralipid solution (Fig. 1c and S2)[34] and was also excluded from the NIR-IIa imaging window.

Live Mouse Brain Imaging in NIR-I, NIR-II and NIR-IIa Regions

We performed non-invasive *in vivo* cerebrovascular fluorescence imaging of healthy C57Bl/6 mice with the same SWNT-IRDye800 conjugates in several spectral windows. A solution of SWNT-IRDye800 was injected intravenously through the tail (see Methods) of a mouse. The head of the mouse with hair shaved off (Fig. 2a) was imaged without craniotomy in the NIR-I (< 900 nm), NIR-II (1.0–1.7 μm) and NIR-IIa (1.3–1.4 μm) regions respectively (pixel size = 78 μm) under an 808-nm laser illumination (Fig. S3). In contrast to the blurry vasculatures imaged in the < 900 nm NIR-I region (Fig. 2b), much sharper images were obtained by detecting longer wavelength photons (Fig. 2c), and the sharpest and highest resolution images of brain vessels were seen in the 1.3–1.4 μm NIR-IIa region (Fig. 2d). Similar to the Intralipid phantom imaging case, rejecting the shorter wavelength < 1.3 μm photons significantly reduced background signals and vessel blurriness caused by scattering, and improved signal/background ratio and imaging quality. The cerebral angiogram taken in the 1.3–1.4 μm NIR-IIa region clearly showed the inferior cerebral vein (labeled as 1), the superior sagittal sinus (labeled as 2) and transverse sinus (labeled as 3) at ~1–2 mm depths under the scalp skin (Fig. S4), along with other cortical vessels in both cerebral hemispheres (Fig. 2d). A 360-degree rotational view of the mouse head was also recorded in the 1.3–1.4 μm NIR-IIa region to show a 3D perspective of the mouse head (Movie S1).

The wavelength dependence of fluorescence imaging of mouse brain can be gleaned by inspecting the extinction spectra of the scalp skin and the cranial bone (i.e., the skull), both of which feature a water overtone vibration absorption peak above ~ 1.4 μm and a declining photon scattering profile (Fig. 2e). To examine the effect of scattering, we plotted reduced scattering coefficients $\mu_s^{'}$ of these tissues versus wavelength λ (Fig. 2f), based on the empirical formulas given in previous literature ($\mu_s^{'}(\text{scalp})=0.11\lambda^{-4}+1.61\lambda^{-0.22}$, where the two terms are attributed to Rayleigh and Mie scattering respectively; $\mu_s^{'}(\text{skull})=0.72\lambda^{-0.65}$; and $\mu_s^{'}(\text{brain tissue})=4.27\lambda^{-2.07}$) [8,35,36]. It can be seen from the plotted scattering profiles that the reduced photon scattering coefficients in the NIR-IIa range (1.54 mm^{-1} for scalp and 1.42 mm^{-1} for skull at 1350 nm) were lower than in the traditional NIR-I window (1.96

mm^{-1} for scalp and 1.99 mm^{-1} for skull at 800 nm). A simple estimate suggested that the lower scattering coefficients in NIR-IIa corresponded to ~47% fewer scattered photons through the scalp and skull than in the NIR-I region based on the measured scalp thickness of 0.7 mm and the measured skull thickness of 0.6 mm. These factors led to drastically improved imaging of mouse cortical vessels underneath the cranial bone in the NIR-IIa region (Fig. 2d vs. 2b).

High Resolution Cerebral Imaging in the NIR-IIa Window

We then used microscopic objectives to image cerebral vessels with high resolution at 15-fold (pixel size ~ 5 μm) and 30-fold (pixel size ~ 2.5 μm) higher magnification than used for Fig. 2. A home-made stereotactic platform was used to eliminate motion of the mouse head and a 3D translational stage with digital readout allowed us to measure the imaging focal depth inside the brain (Fig. 3a&b). Further, chemical separation of large-diameter semiconducting (LS) nanotubes in the HiPCO material (see Methods for separation details) was performed and the LS tubes with fluorescence emission biased towards the favorable 1.3–1.4 μm region were used for brain imaging to optimize signal on the per unit mass basis of the injected nanotube dose (Fig. 3c and S5). We imaged the entire mouse head (Fig. 3d), zoomed into its left hemisphere (Fig. 3e) and then performed microscopic imaging near the location of a cortical vessel branching from the superior sagittal sinus. A typical microscopic image of the brain vessels taken in the 1.3–1.4 μm NIR-IIa region focused at a depth of 2.6 mm below the surface of the scalp (Fig. 3f; depth of focal plane was determined by the axial travel distance of the digitally controlled stage relative to the objective, as described in Methods) revealed many tiny capillary vessels branching from the larger vessels. Cross-sectional intensity profile of one of the capillary vessels in Fig. 3g showed a Gaussian-fitted full width at half maximum (FWHM) of 6.6 μm (Fig. 3g inset). Based on our *ex vivo* measurement of the total thickness of scalp skin, skull and the meninges as ~1.3 mm (Fig. S4), this capillary vessel located at a depth of 2.6 mm was ~ 1.3 mm deep (2.6 mm–1.3 mm) within the brain tissue. This represented the highest resolution non-invasive fluorescence imaging of brain capillary vessels reported to date (see Fig. 3h-k and Fig. S6 for more brain capillaries imaged with 3 different mice at 1–3 mm depths).

Statistical analysis of measured capillary vessel widths revealed an average vessel width of 9.4 ± 2.5 μm, based on 63 different capillary vessels with widths ranging from 5 μm to 15 μm taken from a series of microscopic cerebral vascular images (Fig. S7). The brain imaging depth was limited to < 3 mm for our wide-field epifluorescence microscopic imaging setup. This limit was likely set by the interference from out-of-focus signals, most notably fluorescence from foreground vessels on the path of the laser beam prior to the focal plane.[37] We envisage a two-photon fluorescence microscope with NIR-IIa excitation should solve this problem and generate optically sectioned images with three-dimensional reconstruction of capillary networks to even deeper penetration depths in the brain, using traditional fluorescent dyes excitable around 600–700 nm in the one-photon absorption process.

Dynamic NIR-IIa Fluorescence Imaging of Cerebral Blood Perfusion

Immediately after tail-vein injection of SWNTs into a healthy control mouse (Mouse C1), we performed dynamic brain imaging (frame rate = 5.3 frame per second) and observed the NIR-IIa signal arising from the lateral sulcus on both sides of the cerebrum within 3 s (Fig. 4a & Movie S2), before the interior cerebral vein, the superior sagittal sinus and the transverse sinus started showing up after 4 s owing to the outflow of SWNTs into the venous vessels (Fig. 4b&c). Principal component analysis (PCA) was applied to the time-course images over a time course of ~20 s and discriminated the arterial vessels (red, Fig. 4d) from the venous vessels (blue, Fig. 4e) based on their haemodynamic difference (Fig. 4f).[20,22] The injected SWNTs kept circulating in the blood for at least 3 h post injection, allowing for static imaging in this time window (Fig. S8). We then repeated the study in mice with surgically induced middle cerebral artery occlusion (MCAO) as a model for stroke to the left cerebral hemisphere. After injection of an SWNT solution into a mouse with MCAO (Mouse M1), the right hemisphere exhibited very similar blood flow to the healthy Mouse C1, while the left hemisphere with MCAO showed a marked delay of blood flow revealed by NIR-IIa fluorescence (Fig. 4g-i, Movie S3). PCA analysis of Mouse M1 revealed a more extended venous vessel network (blue) in the right cerebral hemisphere than in the left, and the arterial vessels (red) only showed up in the intact right hemisphere (Fig. 4j-l). Similar results were reproduced with several healthy mice (Fig. S9a-h) and MCAO diseased mice (Fig. S10a-l).

The dynamic NIR-IIa fluorescence imaging allowed us to quantify cerebral blood perfusion by measuring average NIR-IIa intensity in the region of MCAs.[22] In the healthy Mouse C1, the linearly rising fluorescence signals in both cerebral hemispheres had almost identical slopes, suggesting a relative perfusion of ~1 (see SI for perfusion analysis) (Fig. 4m; Fig. S9i&j for repeat). However, in Mouse M1 with MCAO, the relative perfusion in the occluded left hemisphere was only 0.159 (Fig. 4n; Fig. S10m-o for repeat). Another group of mice (n=4) with cerebral hypoperfusion as a model of circulatory shock was imaged (Fig. S11) to reveal a decrease of blood perfusion of ~20% compared to a dramatic decrease of blood perfusion of ~85% in the MCAO group (red bars, Fig. 4o). The data agreed with laser Doppler measurements (blue bars, Fig. 4o). One advantage of NIR-IIa dynamic fluorescence imaging is that it tracks blood flow in a wide-field imaging setup, which allows for simultaneous tracking of blood flow in multiple vessels and could potentially provide a complementary method to two-photon microscopy based blood flow measurement, which performs line scan along the direction of one single vessel at a time with kHz temporal resolution.[38–40]

Discussion

The NIR-IIa fluorescence imaging method is advantageous for brain imaging in terms of high resolution, deep penetration depth and non-invasive nature without the need for craniotomy. Previously, imaging in the traditional NIR-I region (750–900 nm) has observed sub-10 μm capillary vessels at ~350 μm depth with craniotomy to remove scattering extracerebral tissues,[12] much shallower than the imaging depth of >2 mm below the scalp in the NIR-IIa region without craniotomy. This striking difference can be rationalized by considering the highly scattering nature of the brain tissue, with a large scattering coefficient

of ~ 7.49 mm^{-1} at 800 nm versus ~ 2.54 mm^{-1} at 1350 nm (Fig. 2f), suggesting ~10^4 times greater scattered photons in NIR-I than in NIR-IIa through a ~ 2 mm thick brain tissue. Two- and multi-photon microscopy techniques have reported a typical penetration depth of 1–2 mm in the brain tissue, facilitated by highly localized non-linear excitation and detection;[8,13,14,41] but scalp and skull usually need to be removed and replaced with a cranial window,[8,9] or polished and thinned[10,11] to allow for deeper penetration depth. Similarly, the invasive removal of the overlying tissues such as the scalp and the skull is involved for brain angiography with laser speckle contrast imaging (LSCI)[42,43] and optical frequency domain imaging (OFDI),[44] which have been reported to reach a high spatial resolution of ~10 μm *in vivo*.[44,45] To avoid the invasive treatment of the extracerebral tissue, optical coherence tomography (OCT) and photoacoustic microscopy have both shown the capability of visualizing cortical vasculature at the cost of spatial resolution (10–100 μm), unable to resolve sub-10 μm capillary vessels *in vivo*. In light of the possible inflammatory responses such as altered pial blood vessels induced by invasive extracerebral treatment,[10] the NIR-IIa fluorescence based brain angiography provides a completely non-invasive method to visualize the brain vasculature in live mouse with unprecedented resolution and penetration depth.

Although the maximum penetration depth of < 3 mm in this work prevents it from clinical imaging of much deeper vasculature inside the human brain, our new brain imaging method based on the long-wavelength NIR-IIa fluorescence can serve as a non-invasive biomedical imaging tool of understanding the mechanisms of the impaired neurovascular and neurometabolic regulation on both cortical and sub-cortical levels in animal model studies. Besides the cerebrovascular dynamics probed with NIR-IIa fluorescence in this work, we also envisage non-invasive brain imaging of neuronal and/or glial network activity with cellular resolution in live mice using neuronal activity indicators labeled with NIR-IIa fluorophores. In the long term, we anticipate fluorescence imaging using novel, metabolizable fluorophores with even longer emission wavelengths and less scattering to be eventually applied to diagnosis and monitor of cerebral vascular anomaly such as arteriovenous malformation and brain tumor, and other neurovascular disregulations involving rapid modification of cerebral blood flow, such as migraine.

Conclusions

In this work, we explored a new biological transparent sub-window in the 1.3–1.4 μm, i.e., NIR-IIa region and performed non-invasive brain imaging in this window by penetrating through the intact skin and skull. We resolved cerebral vasculatures with a high spatial resolution of sub-10 μm at a depth of >2 mm in an epifluorescence imaging mode. Compare to previous NIR-II work, we found that the 1.3–1.4 μm NIR-IIa window for *in vivo* imaging can further reduce tissue scattering by rejecting shorter wavelength photons than 1.3 μm. The truly non-invasive nature and dynamic imaging capability of NIR-IIa cerebrovascular imaging could allow for high spatial and temporal resolution imaging to follow biological processes in the brain at the molecular scale. Future work will develop novel high quantum yield NIR-IIa fluorophores, 3D *in vivo* imaging through confocal or two photon techniques, all of which could lead to further advances of *in vivo* optical imaging.

Online Methods

A detailed Methods section can be found in the Supplementary Information.

Preparation of biocompatible SWNT-IRDye800 multicolor emitter

Raw HiPCO SWNTs (Unidym) were suspended in an aqueous solution containing 1 wt% sodium deoxycholate by 1 hour of bath sonication. This suspension was then ultracentrifuged at 300,000 g to collect the supernatant, and 0.75 $mg \cdot ml^{-1}$ of DSPE-mPEG(5 kDa) (1,2-distearoyl-*sn*-glycero-3-phosphoethanolamine-N-[methoxy(polyethyleneglycol, 5000)], Laysan Bio) along with 0.25 $mg \cdot ml^{-1}$ of DSPE-PEG(5 kDa)-NH_2 (1,2-distearoyl-*sn*-glycero-3-phosphoethanolamine-N-[amino(polyethyleneglycol, 5000)], Laysan Bio) was added to the supernatant. The resulting suspension was sonicated for 5 min and dialyzed against 1x phosphate buffer saline (PBS) at pH 7.4. These amine-functionalized SWNTs were conjugated with IRDye800 dye molecules. Briefly, the as-made SWNT solution was concentrated down to ~2 μM after removal of excess surfactant through 30-kDa centrifugal filters (Amicon) and was mixed with 0.1 mM IRDye800 NHS ester (LI-COR) dissolved in dimethylsulfoxide (DMSO). The reaction was allowed to proceed for 1 h at pH 7.4 before removing excess IRDye800 by filtration through the 30-kDa filters.

Sorting of LS nanotubes

A 1-cm diameter column filled with 20 ml of ally dextran-based size-exclusion gel (Sephacryl S-200, GE Healthcare) was used to perform diameter separation of HiPCO SWNTs. 2.5 mg of raw HiPCO SWNTs was sonicated in water with 1 wt% sodium cholate (SC) for 1 h, followed by ultracentrifugation at 300,000 g for 30 min. 80% of the supernatant was collected and diluted with same volume of 1 wt% sodium dodecyl sulfate (SDS) solution before adding to the gel column. Metallic SWNTs passed the column directly, while semiconducting SWNTs were trapped. Finally, a 0.6 wt% SC/0.4 wt% SDS mixed surfactant solution was added to wash out and collect the LS nanotubes.

NIR fluorescence spectroscopy of the SWNT-IRDye800 conjugate

NIR fluorescence spectrum was taken using a home-built NIR spectroscopy setup in the 850–1650 nm region. The excitation light was provided by a 160-mW, 808-nm diode laser (RMPC lasers) and filtered by an 850-nm short-pass filter (Thorlabs), a 1000-nm short-pass filter (Thorlabs), an 1100-nm short-pass filter (Omega) and a 1300-nm short-pass filter (Omega). The excitation light was allowed to pass through the solution of SWNT-IRDye800 conjugate in a 1-mm path cuvette (Starna Cells) and the emission was collected in the transmission geometry. The excitation light was rejected using an 850-nm long-pass filter (Thorlabs). The emitted fluorescence was directed into a spectrometer (Acton SP2300i) equipped with a liquid-nitrogen-cooled InGaAs linear array detector (Princeton OMA-V).

Mouse handling, surgery and injection

C57Bl/6 mice were obtained from Taconic Farms. All animal studies were approved by Stanford University's Administrative Panel on Laboratory Animal Care. For induction of MCAO, an incision was made on the left common carotid artery (CCA) and a silicon-coated nylon filament was introduced into the left CCA and threaded forward into internal carotid

artery (ICA) until the tip occluded the origin of the middle cerebral artery (MCA). For induction of cerebral hypoperfusion, only the left external carotid artery (ECA) and common carotid artery (CCA) were ligated. The hair over the scalp was removed using Nair before tail-vein injection and imaging. All mice were anaesthetized before injection using 2 $L{\cdot}min^{-1}$ O_2 gas flow mixed with 3% Isoflurane. For comparative cerebrovascular imaging in different NIR sub-regions, a solution (200 μL) of 0.43 $mg{\bullet}mL^{-1}$ SWNT-IRDye800 was injected. For dynamic NIR-IIa imaging, a solution (200 μL) of 0.43 $mg{\bullet}mL^{-1}$ SWNT-DSPE-mPEG without IRDye800 was injected. A 28-gauge syringe needle was inserted into the tail vein for injection. For steady-state imaging of the mouse brain, injection was done ~5 min before the mouse was placed on the imaging stage. For dynamic imaging, injection was done in the dark when the mouse was already placed on the imaging stage and the InGaAs camera started recording images continuously immediately after the nanotube solution was injected into the tail vein.

NIR fluorescence imaging in different sub-regions

A liquid-nitrogen-cooled, 320 × 256 pixel two-dimensional InGaAs array (Princeton Instruments) was used to take images in all sub-regions of NIR including the NIR-I, NIR-II and NIR-IIa regions. The excitation light was provided by an 808-nm diode laser coupled to a 4.5-mm collimator, and filtered by an 850-nm short-pass filter and a 1000-nm short-pass filter (Thorlabs), with an in-plane excitation power density of 140 $mW{\cdot}cm^{-2}$. The emitted fluorescence was allowed to pass through different filter sets to ensure the images taken in different NIR sub-regions. A lens pair consisting of two achromats was used to focus the image onto the detector with different magnifications (see SI for detailed information for selections of filter sets and lens sets).

Microscopic NIR-IIa imaging of cerebral vessels

High-magnification intravital imaging of cerebral vessels was carried out with a 160-mW, 808-nm diode laser as the excitation source and two objective lens (4× and 10×, Bausch & Lomb) for microscopic imaging. The mouse with scalp hair removed was injected with a solution (200 μL) of 0.22 $mg{\cdot}mL^{-1}$ LS nanotubes and placed on a home-made stereotactic platform fixed on a motorized 3D translational stage with digital position readout (Newport). The resulting NIR photoluminescence was collected using the same 2D InGaAs camera in the NIR-IIa window as aforementioned. The depth of vessels was determined by recording the distance the 3D stage had travelled axially to the objective from focusing on the scalp surface. Snell's law was applied to correct for the actual depth due to refractive index mismatch.[8]

Dynamic cerebrovascular imaging in the NIR-IIa window

The dynamic imaging setup was the same as the aforementioned NIR-IIa fluorescence brain imaging with lower magnification that covered the entire mouse head. The InGaAs camera was set to expose continuously with an exposure time of 100 ms, to which an 87.5-ms overhead time was added to result in a frame rate of 5.3 $frames{\cdot}s^{-1}$. The dynamic-contrast-enhanced images were obtained by loading the first 100 consecutive frames with the MATLAB software for PCA analysis of arterial and venous vessels based on their haemodynamic difference.[20,22,46]

Supplementary Material

Refer to Web version on PubMed Central for supplementary material.

Acknowledgments

This study was supported by grants from the National Cancer Institute of US National Institute of Health to H. D. (5R01CA135109-02), an American Heart Association Innovative Science Award and NIH 1R01NS064517 to C. J. K., and a William S. Johnson Fellowship to G. H. We acknowledge helpful discussions with Prof. John M. Pauly, Dr. Daryl Wong and Dr. Tao Zhang.

References

1. Go AS, et al. Heart Disease and Stroke Statistics-2013 Update A Report From the American Heart Association. Circulation. 2013; 127:E6–E245. [PubMed: 23239837]
2. Schramm P, Schellinger PD, Fiebach JB, Heiland S, Jansen O, Knauth M, Hacke W, Sartor K. Comparison of CT and CT angiography source images with diffusion-weighted imaging in patients with acute stroke within 6 hours after onset. Stroke. 2002; 33:2426–2432. [PubMed: 12364733]
3. Wright SN, Kochunov P, Mut F, Bergamino M, Brown KM, Mazziotta JC, Toga AW, Cebral JR, Ascoli GA. Digital reconstruction and morphometric analysis of human brain arterial vasculature from magnetic resonance angiography. Neuroimage. 2013; 82:170–181. [PubMed: 23727319]
4. Huang CH, Chen CCV, Siow TY, Hsu SHS, Hsu YH, Jaw FS, Chang C. High-Resolution Structural and Functional Assessments of Cerebral Microvasculature Using 3D Gas Delta R-2*-mMRA. Plos One. 2013; 8
5. Flohr TG, et al. First performance evaluation of a dual-source CT (DSCT) system (vol 16, pg 256, 2006). Eur Radiol. 2006; 16:1405–1405.
6. Jacoby C, Boring YC, Beck A, Zernecke A, Aurich V, Weber C, Schrader J, Flogel U. Dynamic changes in murine vessel geometry assessed by high-resolution magnetic resonance angiography: A 9.4T study. J Magn Reson Imaging. 2008; 28:637–645. [PubMed: 18777558]
7. Paulus MJ, Gleason SS, Kennel SJ, Hunsicker PR, Johnson DK. High resolution X-ray computed tomography: An emerging tool for small animal cancer research. Neoplasia. 2000; 2:62–70. [PubMed: 10933069]
8. Horton NG, Wang K, Kobat D, Clark CG, Wise FW, Schaffer CB, Xu C. In vivo three-photon microscopy of subcortical structures within an intact mouse brain. Nat Photonics. 2013; 7:205–209.
9. Svoboda K, Denk W, Kleinfeld D, Tank DW. In vivo dendritic calcium dynamics in neocortical pyramidal neurons. Nature. 1997; 385:161–165. [PubMed: 8990119]
10. Drew PJ, Shih AY, Driscoll JD, Knutsen PM, Blinder P, Davalos D, Akassoglou K, Tsai PS, Kleinfeld D. Chronic optical access through a polished and reinforced thinned skull. Nat Methods. 2010; 7:981–U960. [PubMed: 20966916]
11. Yang G, Pan F, Parkhurst CN, Grutzendler J, Gan WB. Thinned-skull cranial window technique for long-term imaging of the cortex in live mice. Nat Protoc. 2010; 5:201–208. [PubMed: 20134419]
12. Martirosyan NL, Cavalcanti DD, Eschbacher JM, Delaney PM, Scheck AC, Abdelwahab MG, Nakaji P, Spetzler RF, Preul MC. Use of in vivo near-infrared laser confocal endomicroscopy with indocyanine green to detect the boundary of infiltrative tumor Laboratory investigation. J Neurosurg. 2011; 115:1131–1138. [PubMed: 21923240]
13. Theer P, Hasan MT, Denk W. Two-photon imaging to a depth of 1000 microm in living brains by use of a Ti:Al2O3 regenerative amplifier. Optics letters. 2003; 28:1022–1024. [PubMed: 12836766]
14. Kobat D, Horton NG, Xu C. In vivo two-photon microscopy to 1.6-mm depth in mouse cortex. Journal of biomedical optics. 2011; 16:106014. [PubMed: 22029361]
15. Splinter, R.; Hooper, BA. An introduction to biomedical optics. Taylor & Francis; 2007.
16. Frangioni JV. In vivo near-infrared fluorescence imaging. Curr Opin Chem Biol. 2003; 7:626–634. [PubMed: 14580568]

17. Smith AM, Mancini MC, Nie S. Bioimaging: second window for in vivo imaging. Nature nanotechnology. 2009; 4:710–711.
18. Yi HJ, Ghosh D, Ham MH, Qi JF, Barone PW, Strano MS, Belcher AM. M13 Phage-Functionalized Single-Walled Carbon Nanotubes As Nanoprobes for Second Near-Infrared Window Fluorescence Imaging of Targeted Tumors. Nano Lett. 2012; 12:1176–1183. [PubMed: 22268625]
19. Welsher K, Liu Z, Sherlock SP, Robinson JT, Chen Z, Daranciang D, Dai H. A route to brightly fluorescent carbon nanotubes for near-infrared imaging in mice. Nature nanotechnology. 2009; 4:773–780.
20. Welsher K, Sherlock SP, Dai H. Deep-tissue anatomical imaging of mice using carbon nanotube fluorophores in the second near-infrared window. Proceedings of the National Academy of Sciences of the United States of America. 2011; 108:8943–8948. [PubMed: 21576494]
21. Hong G, Wu JZ, Robinson JT, Wang H, Zhang B, Dai H. Three-dimensional imaging of single nanotube molecule endocytosis on plasmonic substrates. Nature communications. 2012; 3:700.
22. Hong G, Lee JC, Robinson JT, Raaz U, Xie L, Huang NF, Cooke JP, Dai H. Multifunctional in vivo vascular imaging using near-infrared II fluorescence. Nature medicine. 2012; 18:1841–1846.
23. Won N, Jeong S, Kim K, Kwag J, Park J, Kim SG, Kim S. Imaging Depths of Near-Infrared Quantum Dots in First and Second Optical Windows. Molecular imaging. 2012; 11:338–352. [PubMed: 22954148]
24. Hong GS, Robinson JT, Zhang YJ, Diao S, Antaris AL, Wang QB, Dai HJ. In Vivo Fluorescence Imaging with Ag2S Quantum Dots in the Second Near-Infrared Region. Angew Chem Int Edit. 2012; 51:9818–9821.
25. Naczynski DJ, Tan MC, Zevon M, Wall B, Kohl J, Kulesa A, Chen S, Roth CM, Riman RE, Moghe PV. Rare-earth-doped biological composites as in vivo shortwave infrared reporters. Nature communications. 2013; 4
26. Tao ZM, Hong GS, Shinji C, Chen CX, Diao S, Antaris AL, Zhang B, Zou YP, Dai HJ. Biological Imaging Using Nanoparticles of Small Organic Molecules with Fluorescence Emission at Wavelengths Longer than 1000 nm. Angew Chem Int Edit. 2013; 52:13002–13006.
27. Dong BH, Li CY, Chen GC, Zhang YJ, Zhang Y, Deng MJ, Wang QB. Facile Synthesis of Highly Photoluminescent Ag2Se Quantum Dots as a New Fluorescent Probe in the Second Near-Infrared Window for in Vivo Imaging. Chem Mater. 2013; 25:2503–2509.
28. Hong G, Lee JC, Jha A, Diao S, Nakayama KH, Hou L, Doyle TC, Robinson JT, Antaris AL, Dai H, Cooke JP, Huang NF. Near-Infrared II Fluorescence for Imaging Hindlimb Vessel Regeneration With Dynamic Tissue Perfusion Measurement. Circulation. Cardiovascular imaging. 2014; 7:517–525. [PubMed: 24657826]
29. Hong G, et al. Ultrafast fluorescence imaging in vivo with conjugated polymer fluorophores in the second near-infrared window. Nature communications. 2014; 5:4206.
30. Chiang IW, Brinson BE, Huang AY, Willis PA, Bronikowski MJ, Margrave JL, Smalley RE, Hauge RH. Purification and characterization of single-wall carbon nanotubes (SWNTs) obtained from the gas-phase decomposition of CO (HiPco process). J Phys Chem B. 2001; 105:8297–8301.
31. O'Connell MJ, Bachilo SM, Huffman CB, Moore VC, Strano MS, Haroz EH, Rialon KL, Boul PJ, Noon WH, Kittrell C, Ma JP, Hauge RH, Weisman RB, Smalley RE. Band gap fluorescence from individual single-walled carbon nanotubes. Science. 2002; 297:593–596. [PubMed: 12142535]
32. Bachilo SM, Strano MS, Kittrell C, Hauge RH, Smalley RE, Weisman RB. Structure-assigned optical spectra of single-walled carbon nanotubes. Science. 2002; 298:2361–2366. [PubMed: 12459549]
33. van Staveren HJ, Moes CJ, van Marie J, Prahl SA, van Gemert MJ. Light scattering in Intralipid-10% in the wavelength range of 400–1100 nm. Applied optics. 1991; 30:4507–4514. [PubMed: 20717241]
34. Curcio JA, Petty CC. The near Infrared Absorption Spectrum of Liquid Water. J Opt Soc Am. 1951; 41:302–304.
35. Bashkatov AN, Genina EA, Kochubey VI, Tuchin VV. Optical properties of human cranial bone in the spectral range from 800 to 2000 nm - art. no. 616310. Saratov Fall Meeting 2005: Optical Technologies in Biophysics and Medicine VII. 2006; 6163:16310–16310.

36. Bashkatov AN, Genina EA, Kochubey VI, Tuchin VV. Optical properties of human skin, subcutaneous and mucous tissues in the wavelength range from 400 to 2000 nm. J Phys D Appl Phys. 2005; 38:2543–2555.

37. White JG, Amos WB, Fordham M. An Evaluation of Confocal Versus Conventional Imaging of Biological Structures by Fluorescence Light-Microscopy. J Cell Biol. 1987; 105:41–48. [PubMed: 3112165]

38. Kleinfeld D, Mitra PP, Helmchen F, Denk W. Fluctuations and stimulus-induced changes in blood flow observed in individual capillaries in layers 2 through 4 of rat neocortex. Proceedings of the National Academy of Sciences of the United States of America. 1998; 95:15741–15746. [PubMed: 9861040]

39. Shih AY, Driscoll JD, Drew PJ, Nishimura N, Schaffer CB, Kleinfeld D. Two-photon microscopy as a tool to study blood flow and neurovascular coupling in the rodent brain. J Cerebr Blood F Met. 2012; 32:1277–1309.

40. Helmchen F, Kleinfeld D. In Vivo Measurements of Blood Flow and Glial Cell Function with Two-Photon Laser-Scanning Microscopy. Method Enzymol. 2008; 444:231–254.

41. Helmchen F, Denk W. Deep tissue two-photon microscopy. Nat Methods. 2005; 2:932–940. [PubMed: 16299478]

42. Dunn AK. Laser Speckle Contrast Imaging of Cerebral Blood Flow. Ann Biomed Eng. 2012; 40:367–377. [PubMed: 22109805]

43. Boas DA, Dunn AK. Laser speckle contrast imaging in biomedical optics. Journal of biomedical optics. 2010; 15

44. Vakoc BJ, Lanning RM, Tyrrell JA, Padera TP, Bartlett LA, Stylianopoulos T, Munn LL, Tearney GJ, Fukumura D, Jain RK, Bouma BE. Three-dimensional microscopy of the tumor microenvironment in vivo using optical frequency domain imaging. Nature medicine. 2009; 15:1219-U1151.

45. Senarathna J, Rege A, Li N, Thakor NV. Laser Speckle Contrast Imaging: theory, instrumentation and applications. IEEE reviews in biomedical engineering. 2013; 6:99–110. [PubMed: 23372086]

46. Hillman EMC, Moore A. All-optical anatomical co-registration for molecular imaging of small animals using dynamic contrast. Nat Photonics. 2007; 1:526–530. [PubMed: 18974848]

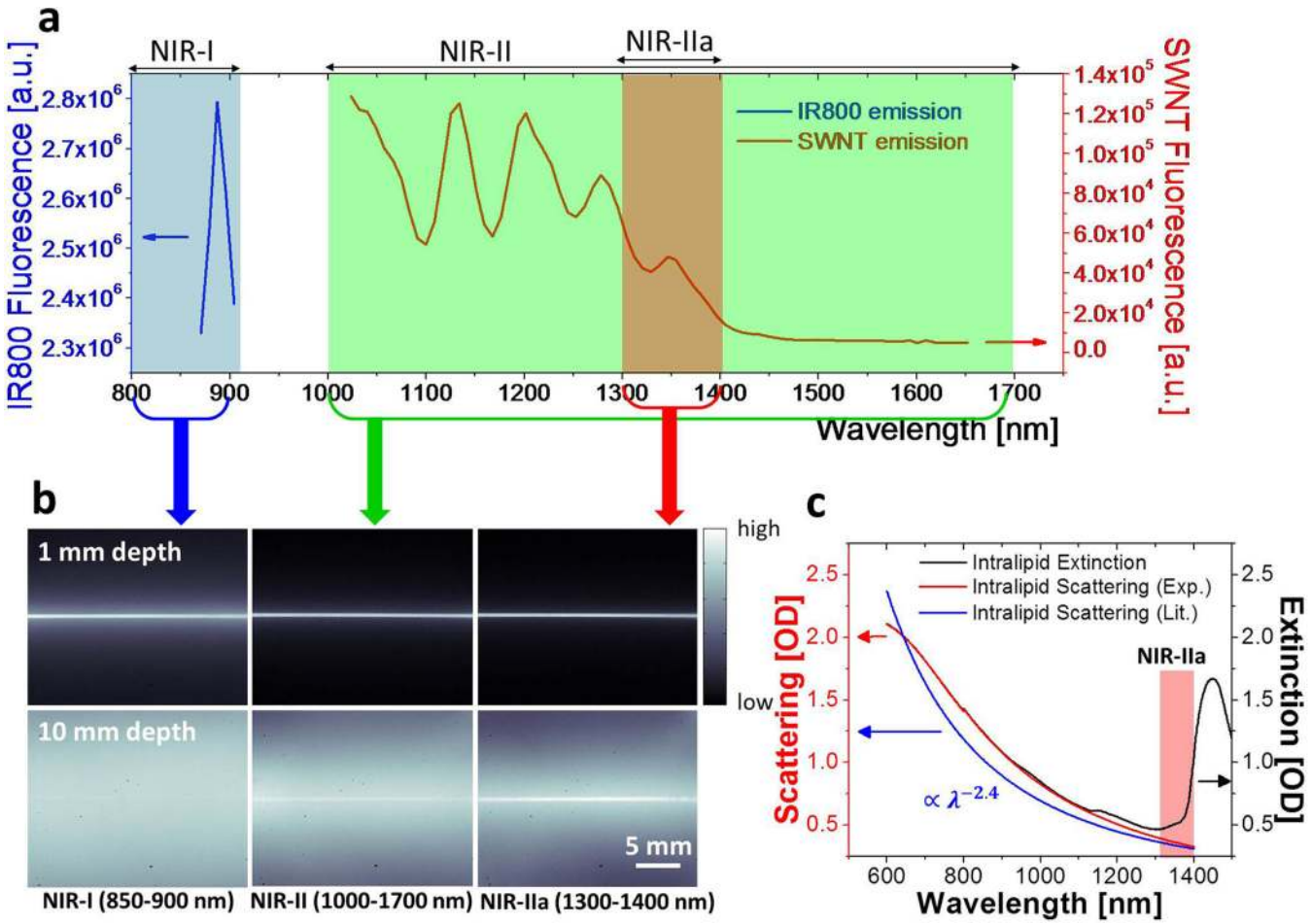

Figure 1.

Imaging in various NIR sub-regions. (**a**) A fluorescence emission spectrum of SWNT-IRDye800 conjugate in the range of 850–1650 nm under the excitation of an 808-nm laser. The emission spectra of IRDye800 and SWNT are plotted under different *y* axis scales to accommodate both into the same graph, due to the much higher fluorescence intensity of IRDye800 than SWNTs. (**b**) NIR fluorescence images of a capillary tube filled with SWNT-IRDye800 solution immersed at depths of 1 mm (top) and 10 mm (bottom) in 1% Intralipid recorded in NIR-I, NIR-II and NIR-IIa regions respectively. (**c**) The extinction spectrum (black curve) and scattering spectrum (red curve, measured by subtracting water and Intralipid absorptions from the extinction spectrum, see Fig. S2) of 1% Intralipid in water with path length of 1 mm measured by UV-Vis-NIR spectrometer, along with reduced scattering coefficient profile (blue) of 1% Intralipid derived from literature.[33]

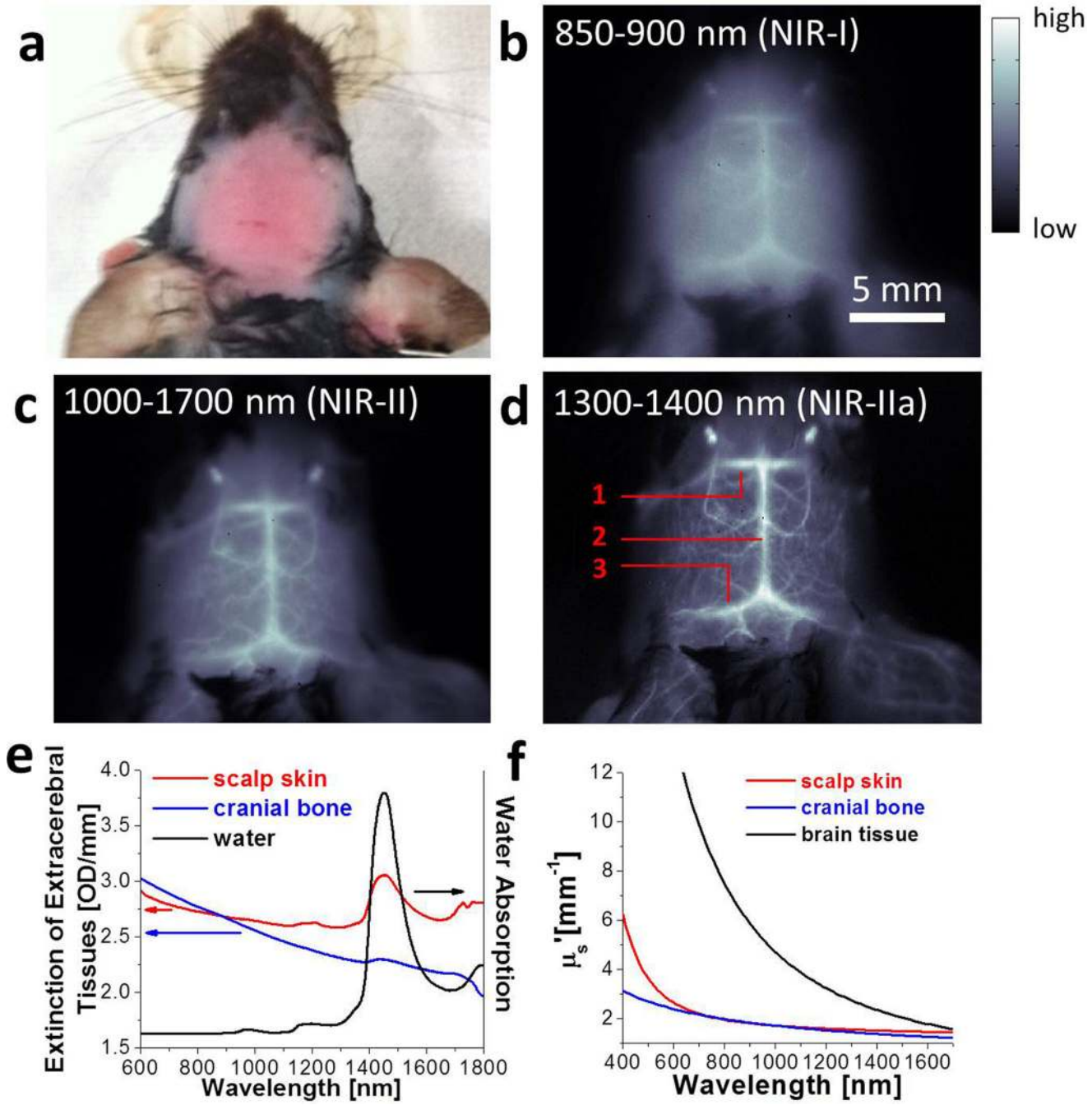

Figure 2.

In vivo mouse brain imaging with SWNT-IRDye800 in different NIR sub-regions. (**a**) A C57Bl/6 mouse head with hair removed. (**b-d**) Fluorescence images of the same mouse head in the NIR-I, NIR-II and NIR-IIa regions. The inferior cerebral vein, the superior sagittal sinus and transverse sinus are labeled 1, 2 and 3 in **d**, respectively. (**e**) Extinction spectra of scalp (red) and skull (blue) along with the water absorption spectrum (black). (**f**) Reduced scattering coefficients μ_s' of scalp skin (red), cranial bone (blue) and brain tissue (black)

plotted against wavelength, based on the previously reported scattering properties for these tissues.[8,35,36]

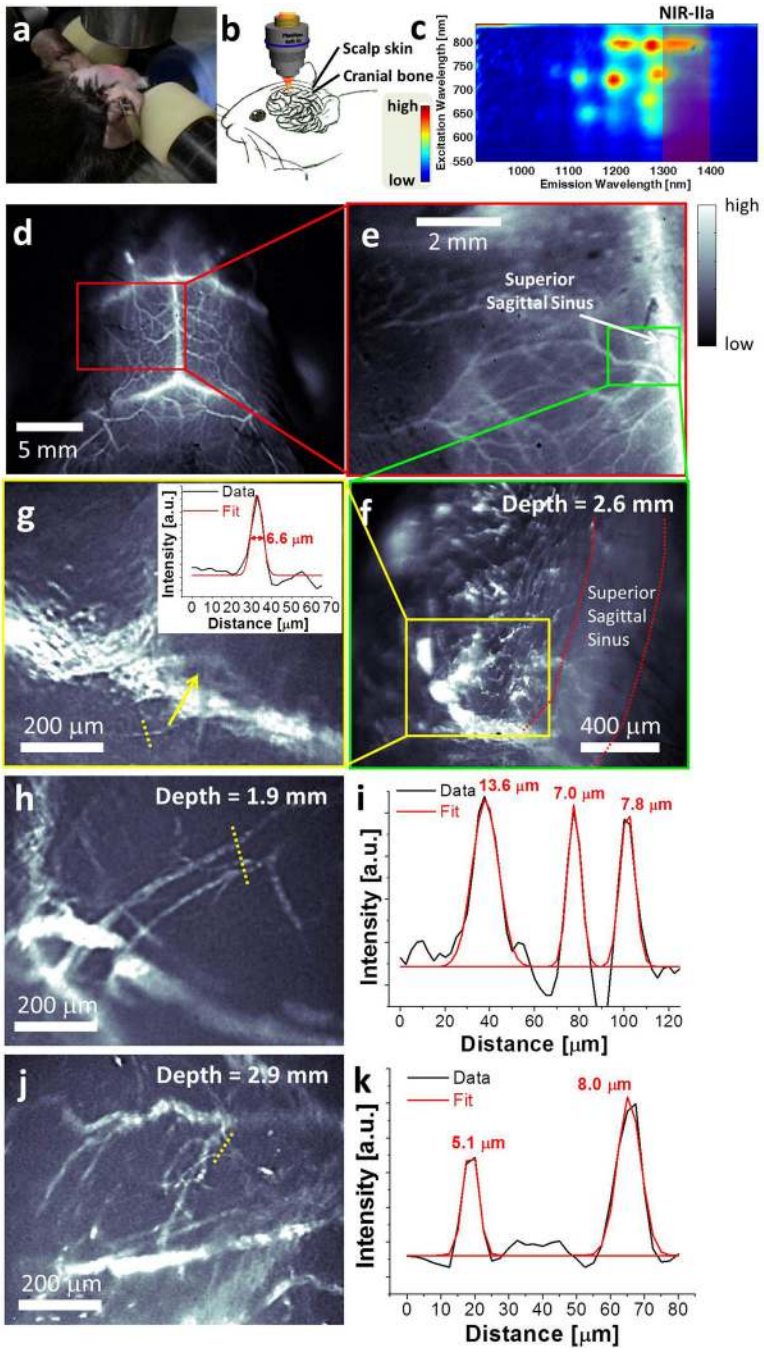

Figure 3.

Non-invasive, high-resolution NIR-IIa fluorescence imaging of mouse brain vasculature. (**a**) A photo showing the stereotactic microscopic imaging setup, where a red laser is used for alignment and shows the beam location. (**b**) A schematic showing the penetration of NIR-IIa fluorescence through brain tissue, skull and the scalp. (**c**) A photoluminescence versus excitation (PLE) spectrum of LS nanotubes in an aqueous solution. The 1.3–1.4 μm NIR-IIa region is shaded red. (**d**) A low-magnification cerebral vascular image taken with a field of view of 25 mm × 20 mm. (**e**) A cerebral vascular image of the same mouse head zoomed

into the left cerebral hemisphere, with a field of view of 8 mm × 6.4 mm. (**f**) A cerebral vascular image of the same mouse head taken using a microscope objective, with a field of view of 1.7 mm × 1.4 mm. The depth of these in-focus vascular features was determined as 2.6 mm. (**g**) A zoomed-in image of a sub-region in **f** taken by a higher magnification objective, with a field of view of 0.80 mm × 0.64 mm. The inset shows the cross-sectional intensity profile (black) and Gaussian fit (red) along the yellow-dashed bar. (**h-k**) Two other high resolution cerebral vascular images with a field of view of 0.80 mm × 0.64 mm taken on another mouse (**h**&**j**), and their cross-sectional fluorescence intensity profiles (black) and Gaussian fit (red) along the yellow-dashed bars (**i**&**k**).

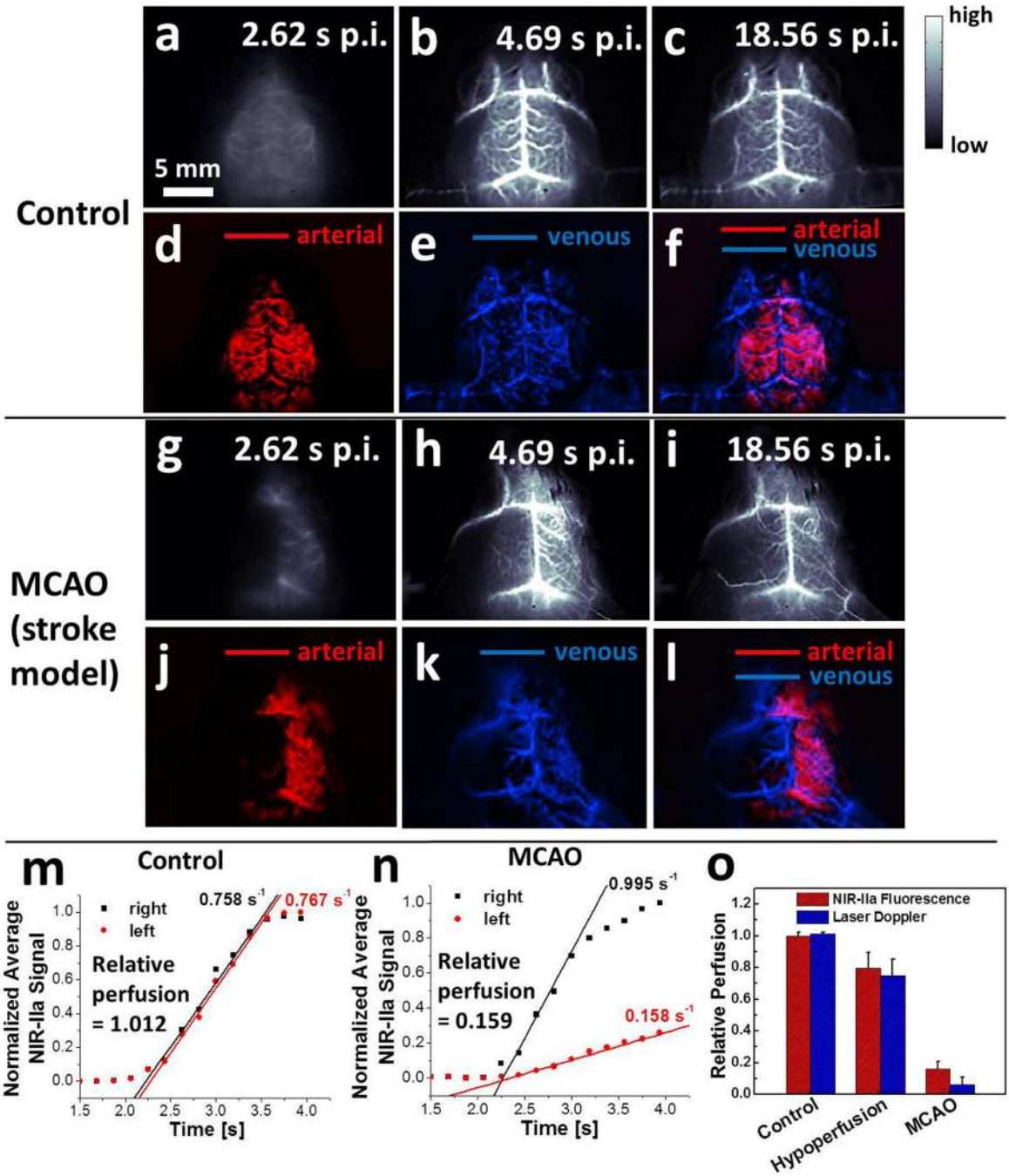

Figure 4.

Dynamic NIR-IIa fluorescence imaging of mouse cerebral vasculature. (**a**-**c**) Time course NIR-IIa images of a control, healthy mouse (Mouse C1). (**d**-**f**) PCA overlaid images showing arterial (red) and venous (blue) vessels of Mouse C1. (**g**-**i**) Time course NIR-IIa images of a mouse with MCAO (Mouse M1). (**j**-**l**) PCA overlaid images showing arterial (red) and venous (blue) vessels of Mouse M1. (**m**-**n**) Normalized NIR-IIa signal in the left (red) and right (black) cerebral hemispheres of Mouse C1 (**m**) and M1 (**n**) versus time. (**o**) Average blood perfusion of the left cerebral hemisphere of control group (n=3), MCAO

group (n=4) and cerebral hypoperfusion group (n=4), measured by NIR-II method (red) and laser Doppler blood spectroscopy (blue). Errors bars reflect the standard deviation of each group.